Quantum transport and mobility spectrum of topological carriers in (001) SnTe/PbTe heterojunctions

D. Śnieżek,[1] J. Wróbel,[2] M. Kojdecki,[3] C. Śliwa,[1] S. Schreyeck,[4] K. Brunner,[4] L. W. Molenkamp,[4] G. Karczewski,[1] and J. Wróbel[1,2,*]

[1]*Institute of Physics, Polish Academy of Sciences, Aleja Lotników 32/46, PL-02-668 Warszawa, Poland*
[2]*Institute of Applied Physics, Military University of Technology, 2 Kaliskiego Str., 00-908 Warsaw, Poland*
[3]*Institute of Mathematics and Cryptology, Military University of Technology, 2 Kaliskiego Str., 00-908 Warsaw, Poland*
[4]*University of Würzburg Am Hubland, Experimental Physics 3, 97074 Würzburg, Germany*

(Received 15 August 2022; accepted 20 December 2022; published 3 January 2023)

Measurements of magnetotransport in SnTe/PbTe heterojunctions grown by the molecular beam epitaxy technique on (001) undoped CdTe substrates were performed. At low magnetic fields, quantum corrections to conductivity were observed that may be attributed to the presence of topological states at the junction interface. For a sample with a 5-nm-thick SnTe layer, the data analysis suggests that midgap states are actually gapped. However, the phase coherence effects in 10 and 20 nm SnTe/PbTe samples are fully explained assuming the existence of gapless Dirac cones. Magnetotransport at higher magnetic fields is described in the framework of mobility spectrum analysis (MSA). We demonstrate that the electron- and holelike peaks observed simultaneously for all SnTe/PbTe heterojunctions may originate from the concave and convex parts of the energy isosurface for topological states—and not from the existence of quasiparticles both carrying negative and positive charges. This interpretation is supported by numerical calculations of conductivity tensor components for gapless (100) Dirac cones, performed within a classical model and based on the solutions of the Boltzmann transport equation. Our approach shows the feasibility of MSA in application to magnetotransport measurements on topological matter.

DOI: 10.1103/PhysRevB.107.045103

I. INTRODUCTION

Topological crystalline insulators (TCIs) are a class of materials in which gapless surface states are protected by crystal mirror symmetry, rather than time-reversal invariance, as in conventional topological insulators (TIs) [1]. Narrow-gap semiconductors SnTe and (Pb,Sn)Te were the first candidates to be declared as members of the new TCI class. It is known that a band inversion in SnTe occurs at the four L points of the bulk Brillouin zone (BZ), therefore exactly four Dirac cones are expected on the boundary planes (001), (111), and (110) for which the required mirror symmetry [2] is preserved. The gapless surface states, with a linear energy dispersion, were indeed observed on (001) and (111) surfaces of SnTe-class materials by angle-resolved photoemission spectroscopy (ARPES) [3,4].

In contrast to conventional topological insulators, gapless surface states of TCIs have much more tunable properties, as it is relatively easy to lower the spatial symmetry of a system. The application of an electric field [5] or uniaxial and biaxial strains can break the symmetry protection and open the gap for Dirac states [6]. Moreover, the presence of multiple Dirac cones may allow construction of novel quantum devices based on the so-called valleytronics [7]. However, the transport studies of topological surface states (TSSs) are difficult in SnTe-class materials because of the strong p-type conductivity of intrinsic holes, with $p \sim 10^{20}$ cm^{-3} [8]. Such unintentional doping is provided by electrically active Sn vacancies [9]. As a result, the chemical potential is anchored deep in the valence band, and conduction through the TSS is masked by bulk conductance.

Therefore, to enhance the surface-to-bulk ratio and to move the Fermi energy towards Dirac points, epitaxial growth of thin ($\lesssim$100 nm) SnTe films is usually performed on several insulating and conducting substrates. In particular, the (111) layers were grown on BaF_2 [10], CdTe [11], and Bi_2Te_3 [12] supporting templates. SnTe films of (001) crystallographic orientation were deposited on BaF_2 [13] and $SrTiO_3$ (STO) insulators [14,15]. Recently, the fabrication of CdTe/SnTe/CdTe quantum wells on GaAs substrates [16] and SnTe/PbTe heterojunctions on STO templates [17,18] was reported. In both cases, the epitaxial layers were grown along the [001] crystallographic direction.

TSSs on the (001) boundary of SnTe are, in the following sense, more interesting than (111) surface states. In the former case, the Dirac points are not located at the $\bar{X}$ point in the Brillouin zone, rather they are slightly shifted along the $\bar{\Gamma}\bar{X}$ direction [2]. Moreover, Fermi surface topology changes as a function of energy (Lifshitz transition), and a Van Hove singularity in the density of states (DOS) is present at the energy corresponding to the cones' tip. To discuss the topology of the SnTe (001) states, Liu *et al.* [19] introduced a low-energy $\mathbf{k} \cdot \mathbf{p}$ model near the $\bar{X}$ point of the BZ. Some results of model

*Corresponding author: wrobel@ifpan.edu.pl

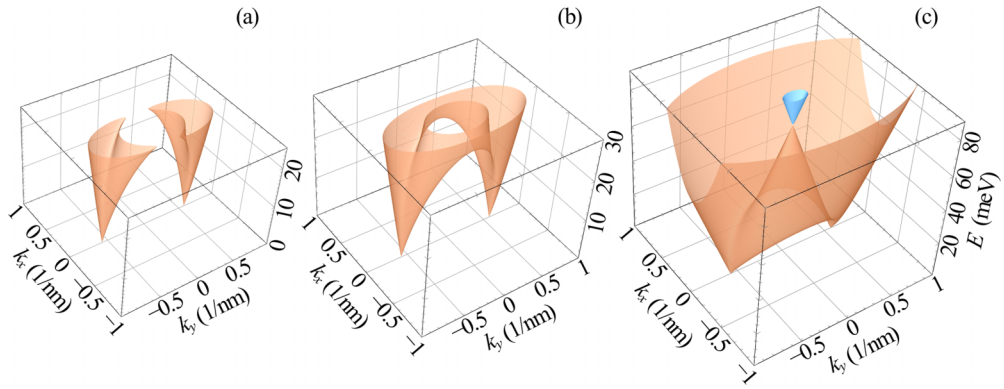

FIG. 1. Energy band structure $E_{\mathrm{H,L}}(\mathbf{k})$ for the (001) surface states. $(k_x, k_y) = (0, 0)$ corresponds to the $\bar{X}$ point of a 2D Brillouin zone [19]. Bands E_{L} with positive energies are plotted up to Fermi level $E_{\mathrm{F}} = 25$ meV (a), $E_{\mathrm{F}} = 30$ meV (b), and $E_{\mathrm{F}} = 90$ meV (c). Subfigures (a) and (b) illustrate the constant energy planes, just below and above a Lifshitz transition, which occurs at $E_{\mathrm{F}} = 26$ meV. For energies $E_{\mathrm{F}} \gtrapprox 75$ meV, the upper band E_{H}, shown as a blue cone in (c), becomes occupied and coexists with bulk states.

calculations are shown in Fig. 1 for three different values of Fermi energy E_{F}.

In this work, we report on magnetotransport measurements of SnTe/PbTe heterojunctions, which were grown by molecular beam epitaxy (MBE) on CdTe/GaAs substrates along the [001] crystallographic direction. At low temperatures and low magnetic fields, we have observed characteristic corrections to the conductivity, related to the interference of electronic wave functions. Data were analyzed using a modified Hikami, Larkin, and Nagaoka (HLN) model, which describes the quantum coherence effects and contains an additional quadratic term accounting for the classical magnetoresistance [20].

Classical magnetotransport at higher fields was described using the so-called mobility spectrum analysis (MSA), which is extremely useful in the case of multicarrier transport [21]. The MSA method was already used for topological materials [22–24]; however, separate peaks detected in mobility spectra are traditionally interpreted as the presence of distinct transport channels. Here we show that electronlike and holelike peaks, observed simultaneously for SnTe/PbTe heterojunctions, originate from the concave and convex parts of the constant energy surface of topological states; see Fig. 1. In other words, both peaks account for the *single-carrier* transport in the *single band* of TSSs.

This claim was supported by the theoretical calculations of the conductivity tensor for carriers described by a Liu *et al.* model. Tensor components σ_{xx} and σ_{xy} were obtained numerically by adopting a McClure approach [25,26], which is based on the solutions of the Boltzmann transport equation. Calculations showed the extremely rich mobility spectra of topological carriers, with a pattern strongly changing with E_{F}. Therefore, the MSA method can in principle be used not only for identification of (001) surface states, but also for localization of the Fermi level relative to the Dirac point and Van Hove singularity.

II. SAMPLE PREPARATION

SnTe/PbTe heterostructures were grown by molecular beam epitaxy (MBE) on (001) oriented CdTe undoped substrates. The growth started from covering the substrate by a few micrometers of epitaxial CdTe, then by depositing a 100-nm-thick PbTe layer, and subsequently a SnTe film of varying thickness (0, 5, 10, and 20 nm); see Fig. 2(a). To keep the two layers homogeneous and prevent mixing of Pb and Sn, MBE growth was carried out at the lowest possible substrate temperature of 230 °C, and the sample was cooled immediately after growth. The entire process was controlled by reflection high-energy electron diffraction (RHEED), showing the excellent quality of the successive layers and that they preserve the orientation of the (001) substrate [25,26]. Based on the oscillations of the RHEED signal, we accurately determined and controlled the thicknesses of PbTe and SnTe layers. Moreover, during the growth of PbTe, the Pb/Te flux ratio was adjusted to assure *n*-type conductivity with an electron concentration of the order of 10^{18} cm^{-3}. The conductivity of SnTe is always *p*-type, as already noted, and in this way we are able to fabricate a *p-n* heterojunction.

Samples of sizes 5×5 mm were cut from such wafers and covered with e-beam resist PMMA. For further processing, we have applied the low-temperature method, developed earlier for II-VI semiconductor quantum wells [27]. In particular, samples were baked for 1 h in 120 °C at lowered pressure to avoid material damage, reduce interdiffusion, and assure a better drying of the resist film. Using electron beam lithography, we have patterned eight-terminal Hall bar devices

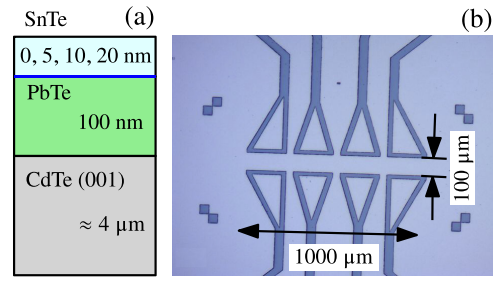

FIG. 2. (a) SnTe/PbTe heterojunction scheme with thicknesses of epilayers indicated. (b) An eight-terminal Hall structure patterned using electron beam lithography with a conducting channel of 1000 µm length and 100 µm width.

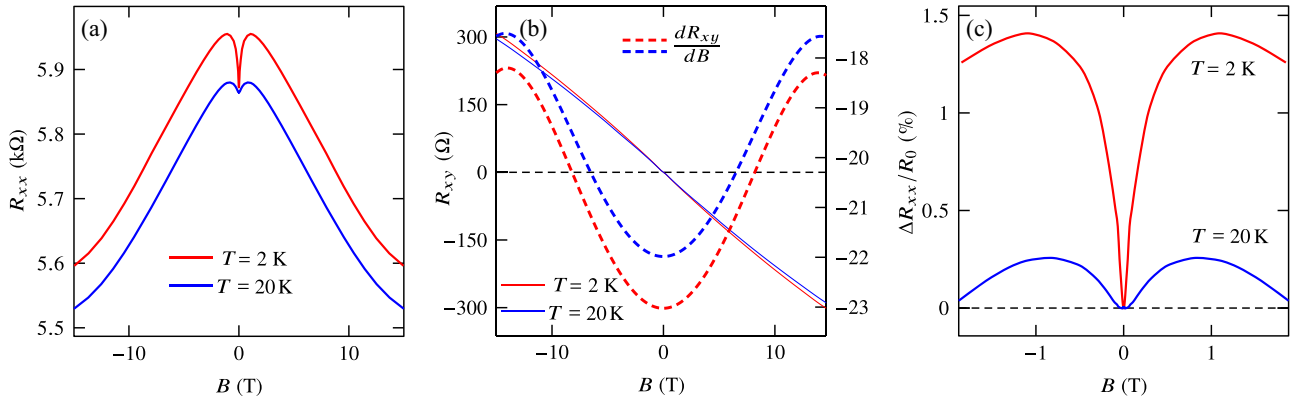

FIG. 3. Magnetotransport measurements for a PbTe layer (0 nm SnTe) at $T = 2$ and 20 K. (a) Longitudinal magnetoresistance R_{xx} vs magnetic field B. (b) Hall resistance R_{xy} (left axis) together with derivatives dR_{xy}/dB (right axis). (c) Relative changes of resistance $\Delta R_{xx}/R_0$ at low magnetic fields, where $R_0 = R_{xx}(0)$.

with a conducting channel size of 1 mm length and 100 μm width [Fig. 2(b)]. After developing, a pattern was etched in 0.06% Br_2 solution in ethylene glycol for 5 min achieving ≈330 nm depth of mesas. Macroscopic contacts were made with silver paint and connected in parallel to both SnTe and PbTe layers. From the same wafers we prepared four-terminal square samples in van der Pauw geometry, not using lithography and avoiding thermal postprocessing. Test measurements showed that the low-temperature method applied for fabrication of Hall-bar samples did not deteriorate the electrical properties of SnTe/PbTe epilayers.

III. MAGNETOTRANSPORT MEASUREMENTS

Patterned Hall bar devices were measured in a He4 cryostat at magnetic fields B up to $B_{\max} = 15$ T, using the constant current (dc) mode. For 10 and 20 nm SnTe/PbTe layers, we used an excitation current of 50 μA. For the 5 nm SnTe/PbTe junction and for a single PbTe layer, which was not covered with SnTe, a smaller current of 5 μA was applied. We measured the longitudinal $R_{xx}(B)$ and vertical (Hall) $R_{xy}(B)$ resistances at temperatures $T = 2,\ 4,\ 8,\ 20,$ and 50 K for 5 and 20 nm SnTe/PbTe junctions. For the PbTe layer and the 10 nm SnTe/PbTe sample, measurements were performed at $T = 2$ and 20 K only. Data were collected for both directions of magnetic field and symmetrized at $\pm B$ points in order to remove contact asymmetry effects. Results are shown in Figs. 3–5.

The Hall resistance data that we show include also the slopes of smoothed $R_{xy}(B)$ curves, which change with magnetic field, indicating the presence of charge carriers with different mobilities. For the mobility spectrum analysis of multicarrier transport in two dimensions, we have calculated conductivity tensor components using standard formulas $\sigma_{xx} = R_{xx}/(R_{xx}^2 + R_{xy}^2)$ and $\sigma_{xy} = R_{xy}/(R_{xx}^2 + R_{xy}^2)$. Additionally, on the right-hand side of the figures, we indicated the relative changes of longitudinal resistance $R_{xy}(B)$ at low magnetic fields. Clearly, the narrow minima caused by weak antilocalization (WAL) are visible for all samples. For PbTe layer, not only WAL, but also the characteristic cusp, induced by weak localization (WL), was observed. It seems that in the case of the PbTe layer, which was not covered by SnTe, quantum corrections to conductivity dominated the whole range of magnetic fields; see Fig. 3(a).

IV. QUANTUM CORRECTIONS TO CONDUCTIVITY

The quantum corrections to the magnetoconductance in 2D systems with strong spin-orbit coupling are commonly described by the Hikami-Larkin-Nagaoka (HLN) model [28], which can be written as follows [20]:

$$\Delta G(B) = \eta\,\Delta G_1 + \eta\,\Delta G_2 - \beta B^2, \tag{1}$$

where

$$\Delta G_1 = \frac{\alpha e^2}{\pi h}\left[\psi\left(\frac{B_\phi}{B} + \frac{1}{2}\right) - \ln\left(\frac{B_\phi}{B}\right)\right], \tag{2}$$

$$\Delta G_2 = -\frac{3\alpha e^2}{\pi h}\left[\psi\left(\frac{4B_{\rm SO} + 3B_\phi}{3B} + \frac{1}{2}\right) - \ln\left(\frac{4B_{\rm SO} + 3B_\phi}{3B}\right)\right]. \tag{3}$$

Here ψ is the digamma function and $\alpha = -1/2$ for the so-called symplectic class. Therefore, the first term is responsible for WAL, and the second one for WL effects. The formula involves characteristic fields $B_\phi = \hbar/(4eL_\phi^2)$ and $B_{\rm SO} = \hbar/(4eL_{\rm SO}^2)$ for scattering channels, L_ϕ and $L_{\rm SO}$ standing for the phase coherence and spin-orbit lengths, respectively. Both terms are multiplied by the parameter $\eta > 0$, which accounts for the *effective number of quantum channels* contributing to transport.

In general, the HLN model contains also the term with $B_{\rm e} = \hbar/(4e\ell_{\rm e}^2)$, where $\ell_{\rm e}$ is the elastic scattering length. We estimated, however, that for electrons in PbTe and holes in SnTe, the mean free paths ℓ_e are very short and fall within the range 1.0–3.0 nm; see Sec. V C. Therefore, for all samples, terms containing $B_{\rm e} \gg B_{\max} = 15$ T are negligible and can be safely ignored. Instead, following [20], we have modified the HLN formula by including an additional quadratic term βB^2, which accounts for the *classical positive magnetoresistance*, of the type described by formula (6), given below. We did not expect, however, that such a single term describes correctly the classical magnetoresistance in the entire range of fields,

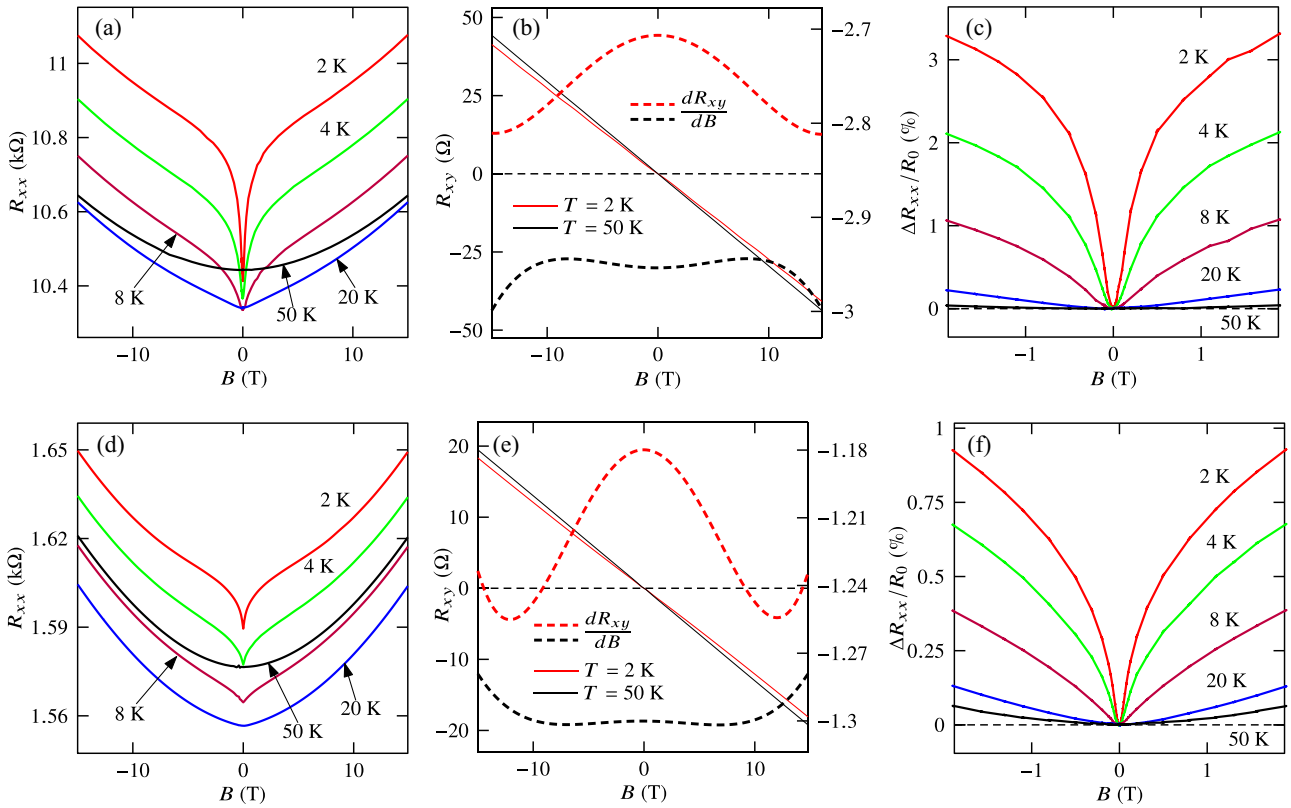

FIG. 4. Results for 5 nm (a)–(c) and 20 nm (d)–(f) SnTe layers at $T = 2,\ 4,\ 8,\ 20,$ and 50 K. (a),(d) Longitudinal magnetoresistance R_{xx} vs magnetic field B. (b),(e) Hall resistance R_{xy} and derivatives dR_{xy}/dB (dashed lines) at $T = 2$ and 20 K. (c),(f) Relative changes of resistance $\Delta R_{xx}/R_0$ at low magnetic fields.

because of multicarrier transport and the nonspherical shape of Fermi surfaces.

Therefore, we have used formula (1) to fit $\Delta G(B)$ to the experimental data for magnetic fields $B < 3$ T only. Characteristic lengths L_ϕ and L_{SO}, together with coefficients η and β, were treated as the fitting parameters. As has already been noticed [29], the complex nature of the HLN model often leads to results that depend on the initial guess if the standard Levenberg-Marquard optimization techniques are used. In our case, we applied the so-called covariance matrix adaptation evolution strategy (CMA-ES)—an iterative method, where in each iteration new candidate solutions are generated in a stochastic way [30]. We hope that this kind of numerical optimization procedure makes the solutions less dependent on the initial values of the parameters being fitted. We used for calculations the implementation of the CMA-ES algorithm, which is available in the Python language environment [31].

A. PbTe layer

Results of the fitting procedures, applied to PbTe layer data, are shown in Fig. 6. We note that values of the parameter β are rather small, which confirms that the classical contribution becomes important only at higher fields and that the

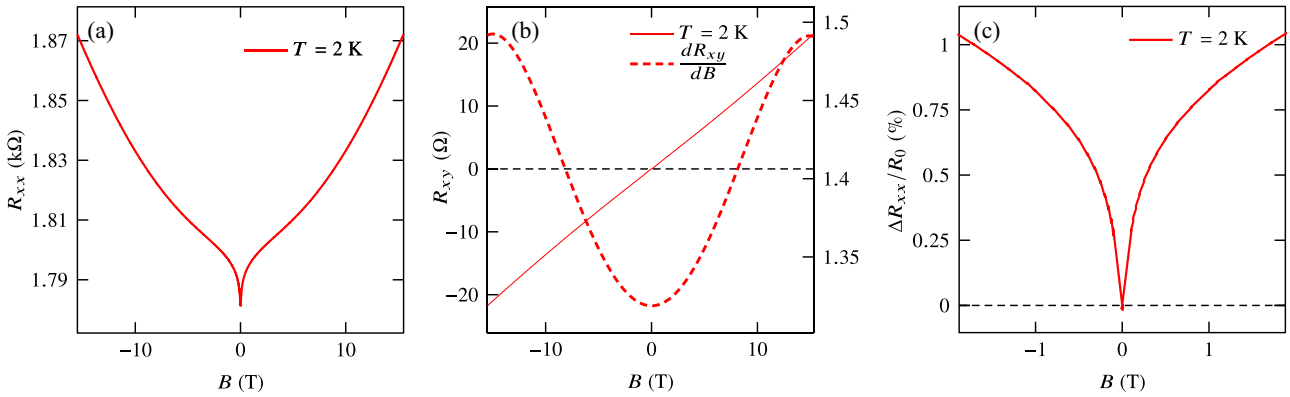

FIG. 5. Results for 10 nm SnTe layer at $T = 2$ K. (a) Longitudinal magnetoresistance R_{xx} vs B. (b) Hall resistance R_{xy} and derivatives dR_{xy}/dB (dashed lines). (c) Relative changes of resistance at low magnetic fields.

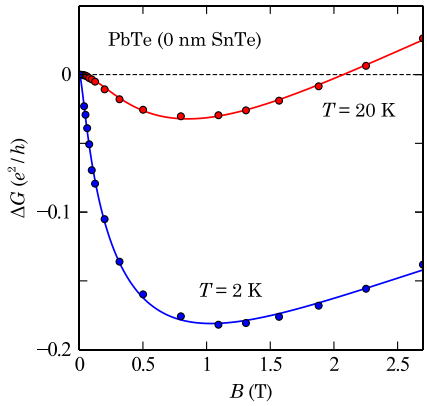

FIG. 6. Measured conductance corrections (points) and fitted curves (lines) for a PbTe layer at temperatures 2 and 20 K. The following parameters were obtained: $\eta = 0.61$, $L_\phi = 120.0$ nm, $L_{SO} = 27.3$ nm, and $\beta = 1.0 \times 10^{-6}$ for $T = 2$ K, and $\eta = 0.97$, $L_\phi = 37.2$ nm, $L_{SO} = 27.0$ nm, and $\beta = 1.3 \times 10^{-5}$ for $T = 20$ K (here β is in e^2/h per Tesla squared units).

$\Delta G(B)$ data for $B > 3$ T are well described by quantum terms only. Data show that the phase coherence length L_ϕ decreased with temperature approximately as $T^{-0.5}$. This may suggest the electron-electron collisions as a phase decay mechanism [32]; however, two data points are probably not enough to definitely identify the dominating inelastic process.

Inelastic processes are important also for a determination of the effective number of quantum channels contributing to transport. For PbTe layers grown along the [001] direction we expect $\eta = 4$, which is the number of equivalent constant energy ellipsoids at L points of the Brillouin zone. In our case, the value of the parameter η is smaller; however, it increases with temperature from 0.61 at 2 K to 0.97 at 20 K. At the same time, the phase coherence length decreases from 120.0 to 37.2 nm, which strongly suggests that the reduction of the parameter η is caused by some coherent processes, which is less effective at higher temperatures.

Most probably, such renormalization results from electron scattering between equivalent ellipsoids [33]. For the first time, the intrasurface valley coupling, which was responsible for reducing parameter η from 2 to approximately 1, was observed for Si inversion layers, which are the two-valley systems [34]. In our case, however, at low temperature, $\eta < 1$, which indicates some additional contribution to quantum corrections, which most probably originates from the weak localization of bulk electrons [35]. Indeed, at $T = 2$ K the phase coherence length L_ϕ is larger than the total thickness of PbTe layer (100 nm). Therefore, we expect some additional quantum interference effects, characteristic for mesoscopic systems. At $T = 20$ K, L_ϕ is reduced and η approaches 1.

As opposed to L_ϕ, the spin-orbit length L_{SO} does not change much with temperature. This result suggests that the Rashba effect is responsible for spin-orbit interactions in a 2D system confined on the PbTe surface. According to [36], the zero-field spin-splitting energy is given by $\Delta_{SO} = \alpha_R k_F$, where α_R is the coupling constant and k_F is the quasimomentum at the Fermi surface. On the other hand, $L_{SO} \propto \Delta_{SO}^{-1}$, therefore the spin-orbit length does not change if the carrier density is constant as a function of temperature, since

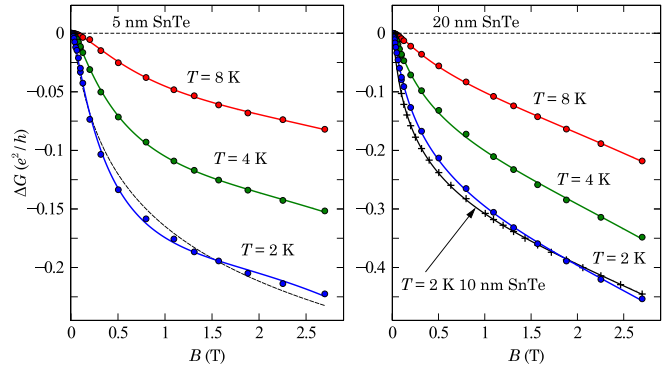

FIG. 7. Conductance corrections $\Delta G(B)$ for a 5 nm SnTe junction (left) and 20 nm SnTe (right) at low temperatures. Data for a 10 nm SnTe junction (at $T = 2$ K) are also included. Measured values are depicted with symbols, fitted curves with lines. Obtained parameters are summarized in Table I.

$k_F = \sqrt{2\pi n}$. This is indeed the case for a 2–20 K range, as is confirmed by mobility spectrum analysis; see Sec. V C. The independent on temperature spin-orbit length L_{SO} has already been reported for PbTe quantum wells grown on (111) planes [29].

B. SnTe/PbTe junctions

The weak antilocalization effect, commonly observed for topological surface states (TSSs), arises from the accumulation of Berry phase π by helical carriers with spin-momentum locking. Therefore, it is assumed that quantum corrections to the conductance of gapless Dirac fermions are simply given by formula (2), with the same value of $\alpha = -1/2$ [37]. For a single SnTe surface, the number of Dirac cones $\eta = 4$ for both (100) and (111) orientations. The results of fitting conductance corrections $\Delta G(B)$ for the SnTe/PbTe junction with the HLN model are shown in Fig. 7.

Initially, we fitted the magnetoconductance data to the simplest version of a modified HLN formula,

$$\Delta G(B) = \eta\, \Delta G_1 - \beta B^2, \tag{4}$$

where ΔG_1 given by Eq. (2), which is commonly used for TSSs. For a 5 nm SnTe/PbTe junction, however, the fit quality was not satisfactory, as is shown with the dashed line in Fig. 7. Therefore, data obtained for a 5 nm SnTe sample have been fitted to Eq. (1). In other words, we have used the same

TABLE I. Fitted parameters for the data obtained for the SnTe sample.

SnTe (nm)	T (K)	η	$L\phi$ (nm)	L_{SO} (nm)	β (T^{-2})
5	2	0.78	77.4	23.7	6.6×10^{-4}
	4	0.57	60.8	19.8	4.8×10^{-4}
	8	0.45	39.7	16.7	3.5×10^{-4}
10	2	0.61	159.8		5.1×10^{-4}
20	2	0.73	115.4		5.6×10^{-4}
	4	0.61	87.1		5.6×10^{-4}
	8	0.49	54.9		5.7×10^{-4}

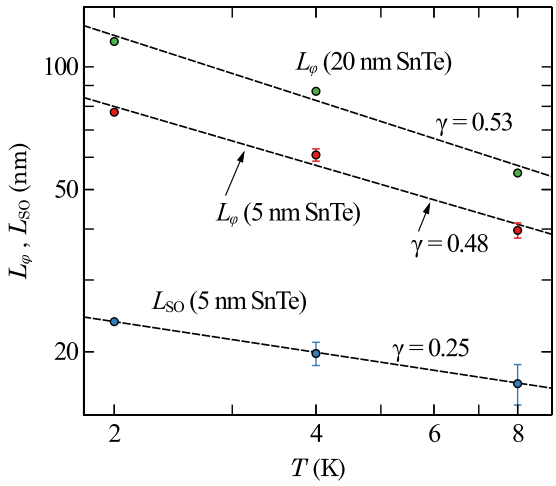

FIG. 8. Characteristic lengths obtained as fitting parameters to the HLN model for 5 nm SnTe/PbTe and 20 nm SnTe/PbTe samples as a function vs temperature T. Dashed lines represent estimated $T^{-\gamma}$ decay.

procedure as for the PbTe sample. The fits are shown with solid lines, and fitted parameters are shown in Table I and plotted as a function of temperature in Fig. 8. Similarly to 2DEG on the PbTe surface, the phase coherence length L_ϕ decreased with temperature approximately as $T^{-0.5}$. Contrary to the PbTe sample, however, parameter L_{SO} also decreased with T, but the decay was slower in comparison to L_ϕ. At low temperatures, L_{SO}, obtained for the 5 nm sample, decreased approximately as $T^{-0.25}$; see Fig. 8.

For 10 and 20 nm SnTe/PbTe junctions, the parameter L_{SO} is not shown in the figures, since for those samples the formula (4) was fully sufficient. Adding the ΔG_2 term did not change the fit quality, therefore the use of Eq. (1) was not justified. This shows that from the point of view of quantum corrections, the 5 nm sample is in some intermediate position between a single PbTe layer and 10 and 20 nm SnTe/PbTe junctions. Nevertheless, the effective number of quantum channels, η, is less than 1 for all junctions and decreases with temperature in the studied range. For example, in the 20 nm SnTe sample, $\eta = 0.73$ at $T = 2$ K and $\eta = 0.49$ at $T = 8$ K. As already discussed, the reduction of the number of channels below the expected limit $\eta = 1$ is most probably caused by the WL contribution coming from bulk carriers.

To verify if this hypothesis holds for 10 and 20 nm SnTe samples, we performed an alternative fit of $\Delta G(B)$ data to the formula $\Delta G(B) = \eta_1 \Delta G_1^{\mathrm{WAL}} + \eta_2 \Delta G_1^{\mathrm{WL}}$, which adds the $\Delta G_1^{\mathrm{WAL}}$ contribution from topological carriers and the ΔG_1^{WL} part from trivial bulk states [10,15]. Here ΔG_1 is again given by Eq. (2), $\alpha = -1/2$ for WAL as before, and $\alpha = +1$ for the WL contribution. The effective numbers of channels η_1, η_2 and phase coherence lengths L_ϕ^{WAL}, L_ϕ^{WL} were treated as fitting parameters. It turned out, however, that final results were very sensitive to the initial values of parameters used by the fit procedure. Nevertheless, from multiple runs of the CMA-ES algorithm, we were able to estimate that $\eta_1 \approx 1$. Therefore, for the alternative fit we used

$$\Delta G(B) = \Delta G_1^{\mathrm{WAL}} + \eta_2 \Delta G_1^{\mathrm{WL}} - \beta B^2, \tag{5}$$

i.e., we fixed $\eta_1 = 1$ for topological states. Final results were practically undistinguishable from the earlier fits to formula (4), which are shown in Fig. 7. For example, we obtained $L_\phi^{\mathrm{WAL}} = 141.8$ nm, $\eta_2 = 0.20$, and $L_\phi^{\mathrm{WL}} = 115$ nm from magnetoconductivity data of the 10 nm SnTe sample at $T = 2$ K. As expected, at low temperatures L_ϕ^{WL} is larger than the thickness of the SnTe epilayer.

We conclude that quantum corrections to conductance for 10 and 20 nm SnTe samples are well described by the HLN model for gapless fermions with the effective number of channels $\eta < 1$ or, alternatively, by the same model with $\eta = 1$ and the additional WL contribution from bulk carriers. The latter approach delegates the $\eta < 1$ problem from topological carriers to trivial states in the bulk. Indeed, from the alternative fit to 20 nm SnTe sample data we obtained $\eta_2 = 0.14$, 0.20, and 0.29 at temperatures $T = 2$, 4, and 8 K, respectively. The effective number of quantum channels, which is less than 1 for the trivial states, was already reported for thin SnTe films and is attributed to the band-edge fluctuations on the epilayer plane [15].

Finally, we mention that the β parameter depends rather weakly on the temperature for all SnTe/PbTe junctions and falls within the (3.5×10^{-4})–(6.6×10^{-4}) range for $T < 8$ K. This demonstrates that the classical contribution βB^2 is much larger for SnTe/PbTe samples than for a single PbTe layer, suggesting the presence of the multicarrier transport—which is actually expected for *p-n* junctions and which is revealed by the analysis of the classical magnetoresistance data.

V. MOBILITY SPECTRUM

Classical transport in topological materials is usually analyzed using Drude expressions for $\sigma_{xx}(B)$ and $\sigma_{xy}(B)$ conductivity tensor components of each charge carrier type [10,11,13,18]. However, this approach is not valid for lead chalcogenides, whose bands are characterized by highly anisotropic effective masses. In particular, for electrons in PbTe, $\gamma = m_\parallel/m_\perp \approx 10$, where $m_\parallel$ is the mass at the L point along [111]-type directions, and $m_\perp$ is a smaller mass for all perpendicular orientations of quasimomentum [38]. Therefore, the Drude model for isotropic bands is no longer applicable. Unfortunately, general expressions for conductivity tensor components of PbTe-like materials, valid at arbitrary magnetic field B, are not known. Analytical formulas for $\sigma_{ij}(B)$ have been developed at the low-field limit only ($\mu B \ll 1$); see [39].

Nevertheless, such low-field formulas can be used to estimate the expected classical component of magnetoresistance data. In particular, for the PbTe layer when B is parallel to the [001] direction, the increase of longitudinal resistance can be expressed as

$$\varrho_{xx}(B) = \varrho_0(1 + \delta^2 \mu_\perp^2 B^2), \tag{6}$$

where ϱ_0 is a zero-field value, $\mu_\perp$ is a mobility of carriers with mass $m_\perp$, and $\delta = 0.271$ for $\gamma = 10$ [40]. Therefore, contrary to the single-band Drude model, a nonzero, positive classical magnetoresistance is expected for PbTe and other lead chalcogenides. Formula (6) was used to calculate $R_{xx}(B) = \varrho_{xx}(B)$ of our PbTe layer. Parameter $\mu_\perp$ was obtained from the slope of $R_{xy}(B)$ data at $B < 2$ T. However, the results are just a rough

estimate, since at least two channels are present in electron transport, as discussed earlier.

To identify different conductive channels, which are responsible for electrical transport in bulk and layered materials, the MSA is usually performed [21]. For that purpose, it is assumed that conductivity tensor components can be expressed as integrals of Drude-like terms, with the $en\mu$ factor replaced by a continuous function $\mathcal{S}(\mu) \geqslant 0$, called the *mobility spectrum*,

$$\sigma_{xx}(B) = \int_{-\infty}^{\infty} \frac{\mathcal{S}(\mu)}{1+\mu^2 B^2} d\mu, \tag{7}$$

$$\sigma_{xy}(B) = \int_{-\infty}^{\infty} \frac{\mathcal{S}(\mu)\,\mu B}{1+\mu^2 B^2} d\mu. \tag{8}$$

This fundamental claim is based on the model of classical transport developed by McClure [25,26], who solved the Boltzmann equation in the presence of a magnetic field and for materials with arbitrary shape of the Fermi surface. In his approach, current carriers travel in reciprocal space on a closed constant energy curve, called a *hodograph*, which lays on a plane perpendicular to the direction of B. Formulas (7) and (8) are valid if the scattering relaxation time τ is constant on the hodograph, which is a *basic assumption* of mobility spectrum analysis. The application of the MSA method lies in finding function $\mathcal{S}(\mu)$ from experimental data.

The shape of the mobility spectrum $\mathcal{S}(\mu)$ provides a deeper insight into transport mechanisms present in the conducting sample, and it delivers more information as compared to the resistivity data alone. Usually, separate spectral peaks are interpreted as distinct conduction channels related to electrons ($\mu < 0$) in the conduction band or holes ($\mu > 0$) in the valence band. An additional piece of information about surface conductivity, impurity bands, or interface transport channels in layered structures can also be inferred from MSA [41].

What is less appreciated, the mobility spectrum may reveal the electronlike and holelike peaks also for *single-band* transport when the Fermi surface is *warped*. As explained in [25,26], convex and concave parts of the hodograph deliver distinct contributions to $\mathcal{S}(\mu)$, which differ by the sign of the related mobility. For example, not only is a strong holelike peak expected, but a weak feature for $\mu < 0$ is expected as well in the mobility spectrum of p-type silicon [42]. It is clear from Fig. 1 that even stronger effects, related to the shape of the Fermi surface, are expected for SnTe topological states, which exist on the (001) plane.

A. McClure model for topological states

We have applied the McClure model of classical transport [25,26] to 2D carriers with dispersion relation $E(k_x, k_y)$ shown in Fig. 1. The model introduces the cyclotron frequency ω_c, defined as $2\pi/T_0$, where T_0 is the period of oscillatory motion performed on the hodograph. Period and frequency were calculated numerically for given energy E and magnetic field B by solving coupled differential equations for $k_x(t)$ and $k_y(t)$, where t is time. From the solution we calculated group velocities $v_x(t)$ and $v_y(t)$ by using the dispersion relation for topological carriers again. Finally, we obtained $\sigma_{xx}(\omega_c)$ and $\sigma_{xy}(\omega_c)$ by applying Fourier transforms, as explained in [25,26]. Tensors for a single hodograph are of course anisotropic, however averaging over all four Dirac-like cones restores the cubic symmetry.

To obtain conductivity tensor components as a function of magnetic field, we took $\mu B = \omega_c \tau$, where τ is the scattering relaxation time, which in general may depend on the energy E and momentum k_z (in our case of 2D carriers, $k_z = 0$). For calculations we used $B_{\max} = 1$ T, and since scattering time is not known, we used an arbitrary value $\tau = 5.523$ ps, just to obtain the condition $\mu B = 1$ for $B \approx 0.5$ T. Details of the calculations will be described elsewhere. Here the representative results for selected values of energy E and temperature $T = 0$ are presented. We have used normalized values of conductivity tensor components $s_{ij} = \sigma_{ij}/\sigma_0$ and dimensionless magnetic field parameter $b = B/B_{\max}$, where $\sigma_0 = \sigma_{xx}(0)$ and $B_{\max}$ is the maximum value of B. By common convention we assumed $\mu < 0$, $\sigma_{xy} < 0$ for electrons and $\mu > 0$, $\sigma_{xy} > 0$ for holes.

Figure 9 shows s_{xx} and s_{xy} calculated for $|E_F| = 25.9$ and 27 meV. The first case corresponds to the situation when the sample is slightly below the Lifshitz transition [see Fig. 1(a)], and the second case corresponds to energies that are above the transition point [Fig. 1(b)]. Insets show closed curves in reciprocal space (hodographs), on which current carriers are orbiting in a magnetic field. Clearly, the obtained data cannot be described by the Drude model of a spherical band. In both cases, σ_{xy} components of the conductivity tensor are rather small, because the convex and concave parts of hodographs give contributions of opposite sign, which partially cancel each other. This mutual cancellation is stronger for energies $E > \delta$, when separate hodographs for "holes" and "electrons" exist.

Especially interesting is the situation for $|E_F|$ slightly below $\delta = 26$ meV, when all hodographs have a crescentlike shape. In that case, "hole" transforms to "electron" and then becomes "hole" again, as a function of time. Moreover, in the real space a current carrier orbits in a clockwise and then an anticlockwise direction or vice versa. This means that the quasiparticle performs a loop, which crosses at a single point on the xy plane, provided $\mu B > 1$ [43]. Moreover, such a complicated band carrier dynamics cannot be described by simply adding two Drude-like terms, one for "electrons" and one for "holes." It was confirmed by the mobility spectrum analysis of calculated conductivity tensors.

B. MSA for topological states

To obtain the mobility spectrum one has to solve the integral Eqs. (7) and (8). This is not an easy task since $\mathcal{S}(\mu)$ often consists of a few narrow peaks, whereas σ_{xx} and σ_{xy} are rather smooth functions of magnetic field B. Therefore, several numerical approaches to MSA exist in the literature [21,41,44]. Here, by replacing integrals (7) and (8) by discrete sums (the trapezoidal rule), we allowed iterative procedures to perform least-squares fits. For the latter task, we adopted constrained optimization algorithms available in the SciPy module of the Python ecosystem [45], requiring that spectrum function $\mathcal{S}(\mu)$ is non-negative. Furthermore, we adopted a special mathematical procedures to avoid spurious splitting of spectral lines, and the obtained results were cross-checked by independent calculations with additional constraints put on

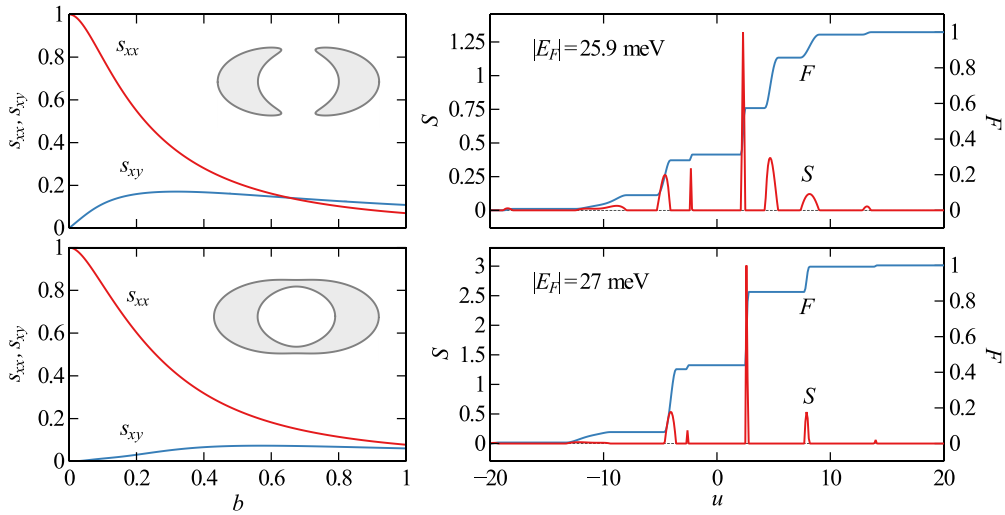

FIG. 9. Normalized conductivity tensor components (left) for Fermi energies 25.9 meV (upper row) and 27 meV (below); insets show schematically the shapes of hodographs. Corresponding mobility spectra S and cumulative conductivity distribution functions F are show on the right. Parameter $b = B/B_{\max}$ is the normalized magnetic field, $u = \mu B_{\max}$ is the normalized mobility. For calculations, we used $\tau = 5.523$ ps and $B_{\max} = 1$ T.

the number of allowed peaks. The details of our numerical approach to MSA are prepared for publication.

We applied our method to the normalized values of conductivity tensor components $s_{ij} = \sigma_{ij}/\sigma_0$, calculated above. We obtained the normalized spectrum $S = \mathcal{S}/(\sigma_0 B_{\max})$ as a function of dimensionless mobility parameter $u = \mu B_{\max}$. From (7) it is clear that for $b = 0$,

$$\int_{-\infty}^{\infty} S(u)\,du = 1. \tag{9}$$

Therefore, in analogy to probability theory, we defined *cumulative conductivity* distribution

$$F(u) = \int_{-\infty}^{u} S(\xi)\,d\xi, \tag{10}$$

which typically shows steplike behavior, where each step height gives a contribution of given carrier "species" to the total conductivity. Results of MSA calculations for topological states are shown in Fig. 9.

Mobility spectrum S obtained for holes with $|E_F| =$ 25.9 meV contains two narrow peaks that are quite symmetric around $u = 0$ and are clearly identified as the contributions arising from convex and concave parts of the sickle-shaped hodograph. However, their shares in the total conductance are not dominant, as can be seen from the $F(u)$ distribution function. For example, the strongest holelike peak for $u \approx 2.3$ amounts to only 26% of the total conductivity. Interestingly, a dominant contribution to electrical transport comes from an additional series of wider maxima, which are observed for higher positive and negative mobilities.

Those *satellite peaks* are related to the higher harmonics of periodic cyclotron motion performed on a strongly warped orbit. Therefore, such a contribution decreases when warping is smaller. Figure 9 shows also the mobility spectrum obtained for $|E_F| = 27$ meV. In this case, we have two separate orbits for carriers moving in opposite directions. Nevertheless, the Drude-like model for electron- and holelike species is again not adequate since strong additional satellite peaks are still detected by MSA. However, the number of "spectral lines" and their positions change considerably, when the Fermi level crosses Van Hove singularity.

What is more, the contribution of higher harmonics does not vanish completely, even when the Fermi energy E_F approaches the Dirac point. Figure 10 shows mobility spectrum S obtained for holes with $|E_F| = 10$ meV. As expected, a strong p-type maximum dominates the conductivity, however an n-type component is also present together with weaker satellite peaks, visible on both electron and hole sides. As indicated in the figure caption, the spectrum was calculated with the same relaxation time as before. Nevertheless, carrier mobilities are much higher as compared to the case when the Fermi energy is larger. This is because of the *linear energy dispersion* close to the Dirac point, where cyclotron frequency ω_c diverges as $1/E_F$. Such dramatic behavior should be taken into account in MSA of topological materials, because it is in stark contrast with normal matter, where ω_c does not depend on the energy at the band edge.

C. Mobility spectrum of SnTe/PbTe junctions

We applied our method of mobility spectrum calculation to analyze experimental data described in Sec. III in order to identify contributions from topological states. Since PbTe and SnTe crystallize in cubic crystal structures with very similar lattice constants, interfaces are only slightly stretched. Therefore, we assumed that such biaxial strain will not introduce a noticeable anisotropy to transport data, which may influence the results of MSA if $\sigma_{xx} \neq \sigma_{yy}$ [46]. We did not, however, expect high-resolution spectra, similar to that visible in Fig. 9, because of two reasons. First, the total conductivity is dominated by bulk (3D) electrons and holes, residing outside the p-n junction. Second, we observed $\sigma_{xx} \gg \sigma_{xy}$ for all available data up to $B_{\max} = 15$ T. This indicates that dominant contributions to electronic transport come from rather low-mobility

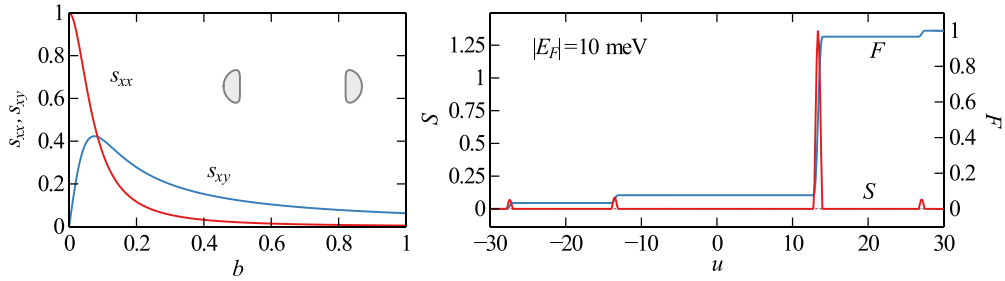

FIG. 10. Normalized conductivity tensor components (left) for Fermi energy 10.0 meV; the inset shows schematically the shape of hodographs. Mobility spectra S and cumulative conductivity distribution functions F are show on the right. We used $\tau = 5.523$ ps and $B_{\max} = 1$ T, the same as in Fig. 9.

($\mu B_{\max} \ll 1$) carrier species, which reduces the resolution of the MSA method.

1. MSA of PbTe layer

The additional difficulty, related to PbTe data, arises because of weak localization effects, which mask the expected positive magnetoresistance in the whole range of magnetic fields. Therefore, to perform MSA, we assumed that $R_{xx}(B) = \rho_{xx}(B)$ is given by the formula (6) with parameters estimated from the $R_{xy}(B)$ curve. From that estimate we calculated conductivity tensor components and then mobility spectra. To increase the weight of $\rho_{xy}(B)$ data, which are not estimated but taken directly from experiment, we fitted the numerical derivative $\partial\sigma_{xy}/\partial B$ instead of σ_{xy}. Results are shown in Fig. 11.

Clearly, two electronlike peaks n_1 and n_2 are visible at temperature $T = 2$ K. The dominant one, observed at mobility $\mu_2 = -80.9$ cm^2/V s, is obviously related to PbTe bulk electrons with sheet carrier concentration estimated to

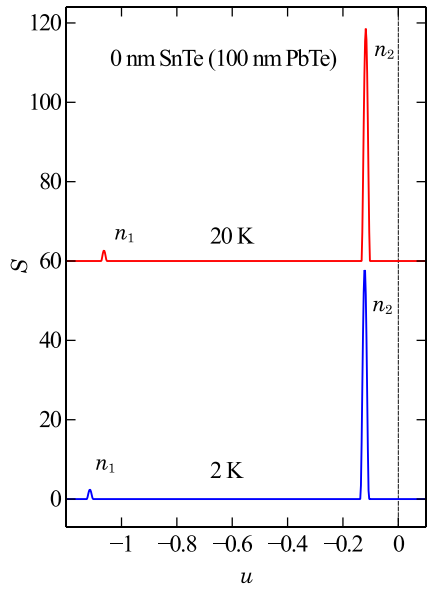

FIG. 11. Normalized mobility spectra $S = \mathcal{S}/(\sigma_0 B_{\max})$ for a PbTe layer at temperatures 2 and 20 K as a function of dimensionless mobility parameter $u = \mu B_{\max}$ ($u = 1.0$ corresponds to $\mu = 666.7$ cm^2/V s, since $B_{\max} = 15$ T). Data for $T = 20$ K are shifted up for clarity. Two electronlike peaks are indicated as n_1 and n_2.

$n_2 = 3.26 \times 10^{13}$ cm^{-2}. The weaker peak, detected for much higher electron mobility $\mu_1 = -743$ cm^2/V s, is apparently related to the 2D electron gas (2DEG) with density $n_1 = 1.07 \times 10^{11}$ cm^{-2}, which is responsible for WL and WAL effects, as discussed before. Most probably, 2DEG resides at the free PbTe surface, as no quantum transport was reported for PbTe/CdTe interfaces grown on (100) substrates [47]. Using well-known expressions for conductivity and density-of-states effective masses [38], we have estimated elastic mean free paths for bulk (n_2) and surface (n_1) electrons as $\ell_2 = 1.02$ nm and $\ell_1 = 1.33$ nm, respectively. Both values are similar and rather small, which suggests the presence of a structural disorder, which significantly reduces the mobility of carriers.

Figure 11 shows also the mobility spectrum for $T = 20$ K, which looks very similar to the results obtained at lower temperature. The widths and heights of the observed peaks are almost unchanged, which indicates that both carrier densities only weakly change with the temperature. With regard to mobilities, μ_2 for bulk electrons is also almost unchanged, whereas the mobility of 2DEG is slightly reduced to $\mu_1 = -709$ cm^2/V s. Nevertheless, the temperature dependence of layer conductivity components is rather weak in the range 2–20 K.

The physical origin of the two-dimensional conduction, described by parameters n_1 and μ_1, is not known. Most probably, the presence of 2DEG is related not only to classical surface states but also to states associated with molecules chemically absorbed from air. In particular, it is known that oxygen molecules draw electrons from the bulk of the semiconductor via oxidation processes. Therefore, a thin insulating layer may be formed and acts as a confining barrier for electrons on the free surface of n-PbTe [48].

2. MSA for SnTe/PbTe junctions

For SnTe/PbTe junctions we did not observe weak localization, which dominated $R_{xx}(B)$ data for PbTe layer. Instead, we observed a positive magnetoresistance and the temperature-dependent narrow minima at low magnetic fields, related to WAL. Therefore, to calculate components of the classical conductivity tensor, we replaced low-field R_{xx} data (dominated by quantum effects) with the parabolic fit. Magnetoresistance data for higher fields, i.e., for $|B| \gtrsim 2$ T, were not fitted and were taken directly from experiment. With regard to the Hall resistance $R_{xy}(B)$, data were not fitted nor modified, even at the low-field range, since the corrections

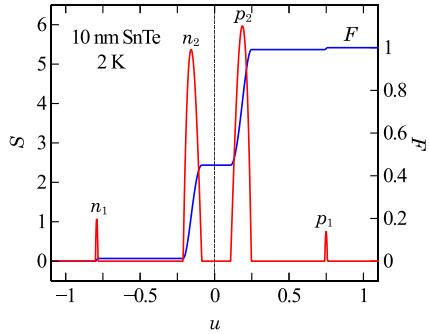

FIG. 12. Normalized mobility spectrum S and steplike cumulative conductivity distribution functions F for a 10 nm SnTe/PbTe junction, temperature $T = 2$ K. From the step height the following averaged parameters were estimated: electronlike: $\mu_1 = -528$ cm^2/V s, $n_1 = 10^{11}$ cm^{-2}, $\mu_2 = -105$ cm^2/V s, $n_2 = 1.45 \times 10^{13}$ cm^{-2}, and holelike: $\mu_1 = +500$ cm^2/V s, $p_1 = 10^{11}$ cm^{-2}, $\mu_2 = +125$ cm^2/V s, $p_2 = 1.47 \times 10^{13}$ cm^{-2}.

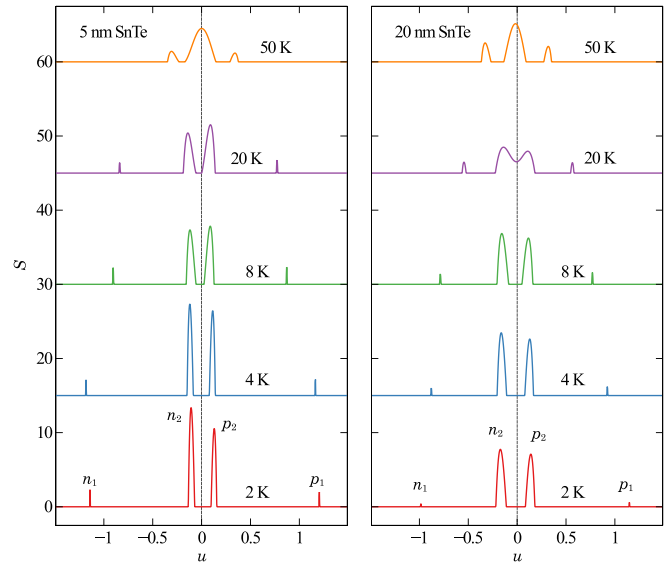

FIG. 13. Mobility spectra for a 5 nm SnTe/PbTe and a 20 nm SnTe/PbTe junction as a function of temperature in the 2–50 K range.

related to quantum interference do not contribute to the Hall effect [49,50], and the quantum effects related to electron-electron interactions (EEIs) are negligible in our case. Indeed, for the EEI effect, the normalized correction to the Hall coefficient is proportional to the relative change of sheet resistance $\Delta R_{xy}/R_{xy} = \xi\ \Delta R_{xx}/R_{xx}$, where $0 < \xi < 2$ indicates the coexistence of EEI and W(A)L effects [51]. By direct comparison, we observed that for our data $\xi \to 0$, which means that quantum corrections are dominated by interference phenomena.

The $\sigma_{xx}(B)$ and $\sigma_{xy}(B)$ experimental curves calculated in this way were then used to obtain the mobility spectra. Results for the 10 nm SnTe junction at a temperature $T = 2$ K are shown in Fig. 12. As expected, two dominant contributions are observed, which corresponds to bulk electrons in PbTe (n_2) and bulk holes in SnTe (p_2) layers. However, the widths of both spectral peaks are much larger as compared to the n_2 line shown in Fig. 11 for a single PbTe layer. We believe that the dominant spectral lines are wider for SnTe/PbTe samples due to the formation of the *p-n* heterojunction at the interface. Electron and hole densities vary across the junction and the same may apply to mobilities, leading to the spread of parameters and spectral broadening. Interestingly, the total sheet densities n_2 and p_2 are quite similar; see Fig. 12. However, if the thicknesses of PbTe (100 nm) and SnTe (10 nm) layers are taken into account, one obtains $n_2^{3D} = 1.45 \times 10^{18}$ cm^{-3} and $p_2^{3D} = 1.47 \times 10^{19}$ cm^{-3} for bulk carrier concentrations, which differ considerably.

MSA shows that the bulk densities are not the only contributions to conductivity for SnTe/PbTe samples. The additional *n*-type (n_1) and *p*-type (p_1) peaks are clearly observed. We attribute *them both* to the topological states, which live at SnTe/normal matter interfaces and which are responsible for the weak antilocalization effect. First, the n_1 contribution cannot be connected with a free surface of PbTe, which is not exposed to air but is buried in the *p-n* junction. Second, the formation of a 2D hole gas on *p*-SnTe, similar to 2DEG observed on a surface *n*-PbTe, is not expected. The SnTe surface is not capped and probably also oxidized, however the density of holes is so high ($\sim 10^{19}$ cm^{-3}) that the formation of an insulating layer is not expected. Without such a barrier, the existence of a surface accumulation (or inversion) layer is not likely here because of the high dielectric constant ($\epsilon = 1200$). The strong screening of surface charges limits band bending to a few meV [13], which is much less then the estimated Fermi energy E_F.

Therefore, the two satellite peaks n_1 and p_1 are not related to the conventional 2D transport in a trivial semiconductor. As discussed in Sec. V A, the shapes of constant energy contours on the (001) surface result in electronlike and holelike contributions to the mobility spectrum of SnTe topological states. Moreover, this observation is valid in a relatively wide range of Fermi energies, from $|E_F| \approx 10$ meV up to $|E_F| \approx 75$ meV, when inner and outer Dirac cones with the same chirality develop. Our estimations show that at least for the *p-n* junction area, the energy of SnTe surface carriers falls within that range. Therefore, we interpret the simultaneously observed peaks n_1 and p_1 as the signatures of nontrivial chirality of topological states. This conclusion is supported by the temperature dependence of mobility spectra, which was studied for 5 nm SnTe and 20 nm SnTe heterojunctions in the temperature range 2–50 K. Results are shown in Fig. 13.

A much stronger temperature dependence is observed as compared to PbTe layer data, which did not change much from 2 to 20 K; see Fig. 11. For PbTe, the electron density n_1 of 2DEG increased by 7% and the absolute value of mobility μ_1 decreased by 5% only. In contrast, for SnTe/PbTe junctions, the already large widths of peaks n_2 and p_2, which are related to bulk carriers, increased further with temperature. At $T = 20$ K, the dominant spectral lines started to overlap and eventually merge at $T = 50$ K, forming a broad peak, which spans over positive and negative mobilities. The satellite spectral lines n_1 and p_1 also changed considerably with T. For a 20 nm SnTe sample, electronlike density n_1 increased 33 times and the absolute value of mobility μ_1 decreased by almost 50% when the heterojunction was warmed from 2 to

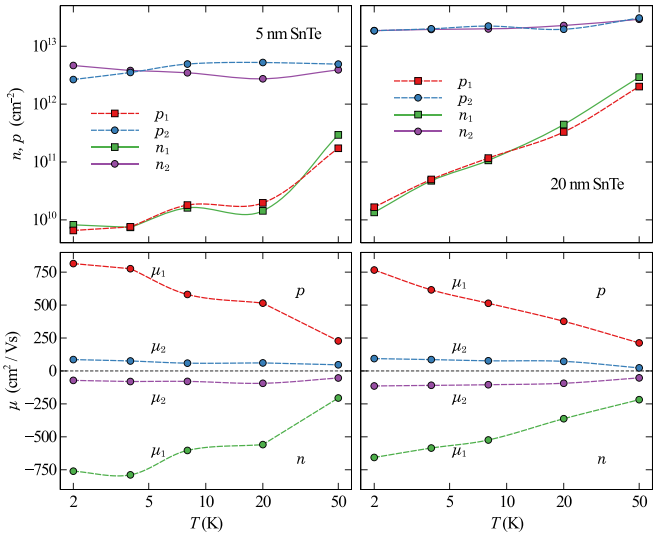

FIG. 14. Results of MSA analysis performed for 5 nm SnTe/PbTe (left) and 20 nm SnTe/PbTe (right) junctions. The upper part shows 2D densities of electronlike (n_1, n_2) and holelike (p_1, p_2) contributions as a function of temperature T. Below, the corresponding mobilities (peaks positions) are shown. By convention, μ for electronlike excitations are negative.

20 K. This is in stark contrast with 2DEG peak n_1, observed for the PbTe layer. The temperature dependence of MSA parameters, obtained for SnTe/PbTe junctions, is summarized in Fig. 14.

The upper part shows estimated sheet densities of electronlike and holelike contributions. The bulk carrier concentrations, marked with circles, did not change much with temperature, as expected. For a 20 nm sample, parameters n_2 and p_2 slightly increased with temperature, whereas for a 5 nm sample, changes were larger but not monotonic. The same observations apply for positive and negative mobilities of majority carriers μ_2, shown in the lower part of Fig. 14. As already mentioned, the widths of mobility peaks increased with temperature, but their positions also did not change considerably. Only at $T = 50$ K have the absolute values of μ_2 markedly decreased and the peaks merged. In spite of broadened spectral lines, the majority carriers in SnTe/PbTe junctions are characterized by relatively small values of mobilities with a weak temperature dependence, very much as bulk electrons in the PbTe layer.

However, the estimated bulk densities of electrons in SnTe/PbTe heterojunctions are considerably smaller than those in the single PbTe layer. At temperature $T = 2$ K we obtained $n_2^{3D} = 1.45 \times 10^{18}$ and 1.87×10^{18} cm^{-3} for 10 and 20 nm samples, respectively, as compared to $n_2^{3D} = 3.26 \times 10^{18}$ cm^{-3} in the PbTe layer. For a 5 nm SnTe/PbTe sample, which has the largest zero-field resistance, this discrepancy is even more dramatic, since $n_2^{3D} = 10^{18}$ cm^{-3}. One possible explanation is that part of each PbTe layer was depleted due to the formation of the p-n junction, and the effective widths were smaller than the nominal 100 nm value used in the calculations. Secondly, the McClure model, which is the foundation of the MSA method, was developed for possibly multicarrier but homogeneous samples. Here, we studied the layered structures with a planar heterojunction and surface conduction, with unknown vertical distribution of electrical current. Therefore, the calculated carrier concentrations may differ from actual ones.

Nevertheless, the quantitative parameters, obtained for electronlike and holelike surface conduction, are consistent for all SnTe/PbTe samples. Figure 14 shows that parameters p_1 and n_1 increase with temperature and both values change in-parallel, which strongly suggests that they belong to the same entity. If they were just the hole and electron concentration of distinct 2DEG systems, such a similarity would be less probable since our multilayer structures are not symmetric along the growth direction. The same applies to μ_1 parameters for electronlike and holelike peaks. Their absolute values decrease with temperature with almost exactly the same rates. The mobility and the density of electrons on the PbTe surface behave differently. This confirms that most probably, peaks p_1 and n_1 belong to the concave and convex parts of the single hodographs, of a type shown in Fig. 9 for topological states. The increase of p_1 and n_1 parameters with temperature can be explained if we assume that at $T = 2$ K the Fermi level E_F is located slightly below the Lifshitz transition energy E_S. Therefore, at higher temperatures, E_F moves towards a van Hove singularity in the density of states, and the conductance related to topological carriers increases.

If this is true, one may ask a more general question: Is the standard MSA approach applicable to TSSs? Maybe, instead of a Drude expression $\sigma = en\mu$, a more general formula $\sigma(E) = e^2\mathcal{D}D(E)$ should be used, where $\mathcal{D}$ is the diffusion coefficient and $D(E)$ is the density of states. Such an expression is far more generally applicable and provides better descriptions for materials such as topological insulators, where the meaning of effective mass and mobility is somehow unclear [52].

VI. CONCLUSIONS AND SUMMARY

The SnTe/PbTe junction at low temperatures is a so-called type-II heterostructure, with the valence-band edge of SnTe located higher than the bottom of the conduction band in PbTe [53]. Due to the large hole density, it is expected that electrons diffuse across the interface, SnTe bands bend downward, and the chemical potential is shifted towards the energy gap [17]. Moreover, due to the lattice mismatch, the SnTe/PbTe heterojunction is strained and the resulting in-plain strain is compressive for PbTe and tensile for SnTe layers. As a result, for (001) junctions, the positive band offset is reduced. For sufficiently large strain, the band gap is not broken anymore [54], which in turn promotes the formation of midgap gapless states with linear dispersion [55].

Biaxial strain influences also the 2D band structure of topological carriers. The tensile distortion of thin (100) SnTe film shifts the Dirac points in reciprocal space and eventually opens the hybridization gap [56]. Such a situation may have arisen for the 5 nm SnTe/Pbte sample, since in that case the quantum corrections to conductance are better described by the formula given by Eq. (1), which is valid for gapped states. Another possibility, which explains the coexistence of WAL and WL effects for this sample, is the formation of trivial Volkov-Pankratov massive states, which are predicted

in wide enough junctions due to the presence of an electric field [55,57].

The phase coherence effects, observed for 10 and 20 nm SnTe/PbTe samples, were fully described by a simpler Eq. (4), which is valid for gapless states. Probably, the tensile strain was more relaxed for thicker SnTe layers, hybridization did not occur, and the gap remained broken. The effective number of quantum channels, η, was reduced for all devices, presumably by the strong intervalley coherent scattering. For all samples, the parameter η was further reduced due to the contribution from the weak localization effect, which is expected for bulk but mesoscopic SnTe and PbTe layers.

For SnTe/PbTe junctions, the mobility spectrum analysis (MSA) revealed the presence of bulk electrons from the PbTe layer and bulk holes from the SnTe layer, as expected. Additionally, the weak holelike and electronlike peaks were observed for higher mobilities, always in pairs, on symmetrical positions around the $\mu = 0$ point. The distance between those peaks decreased with temperature, whereas their density parameter increased. The additional peak pairs were interpreted as the mobility spectrum of carriers occupying the *single topological band*, with the Fermi level pinned in the vicinity of the Lifshitz transition ($E_S = 26$ meV), where the density of states is very large. This conclusion is supported by numerical calculations of the conductivity tensor components for the energy band shown in Fig. 1 using the McClure model of classical transport.

ACKNOWLEDGMENTS

We acknowledge Krzysztof Dybko for the useful discussions. The research in Poland was supported by the National Science Centre (NCN) through the Project No. 2021/41/B/ST3/03651 and in Germany by the Deutsche Forschungsgemeinschaft (DFG) through the program SFB 1170 "ToCoTronics." Work was also partially supported by the Polish National Science Center Grants No. P-376/M and No. DEC-012/07/B/ST3/03607. MSA calculations have been performed thanks to the support of Polish Ministry of Higher Education through the program "Regional Initiative of Excellence," Grant No. 014/RID/2018/19.

[1] L. Fu, Phys. Rev. Lett. **106**, 106802 (2011).
[2] T. H. Hsieh, H. Lin, J. Liu, W. Duan, A. Bansil, and L. Fu, Nat. Commun. **3**, 982 EP (2012).
[3] P. Dziawa, B. J. Kowalski, K. Dybko, R. Buczko, A. Szczerbakow, M. Szot, E. Lusakowska, T. Balasubramanian, B. M. Wojek, M. H. Berntsen, O. Tjernberg, and T. Story, Nat. Mater. **11**, 1023 EP (2012).
[4] S.-Y. Xu, C. Liu, N. Alidoust, M. Neupane, D. Qian, I. Belopolski, J. D. Denlinger, Y. J. Wang, H. Lin, L. A. Wray, G. Landolt, B. Slomski, J. H. Dil, A. Marcinkova, E. Morosan, Q. Gibson, R. Sankar, F. C. Chou, R. J. Cava, A. Bansil *et al.*, Nat. Commun. **3**, 1192 EP (2012).
[5] J. Liu, T. H. Hsieh, P. Wei, W. Duan, J. Moodera, and L. Fu, Nat. Mater. **13**, 178 (2014).
[6] Y. Okada, M. Serbyn, H. Lin, D. Walkup, W. Zhou, C. Dhital, M. Neupane, S. Xu, Y. J. Wang, R. Sankar, F. Chou, A. Bansil, M. Z. Hasan, S. D. Wilson, L. Fu, and V. Madhavan, Science **341**, 1496 (2013).
[7] L. Zhao, J. Wang, B.-L. Gu, and W. Duan, Phys. Rev. B **91**, 195320 (2015).
[8] K. Dybko, M. Szot, A. Szczerbakow, M. U. Gutowska, T. Zajarniuk, J. Z. Domagala, A. Szewczyk, T. Story, and W. Zawadzki, Phys. Rev. B **96**, 205129 (2017).
[9] J. N. Zemel, J. D. Jensen, and R. B. Schoolar, Phys. Rev. **140**, A330 (1965).
[10] R. Akiyama, K. Fujisawa, R. Sakurai, and S. Kuroda, J. Phys.: Conf. Ser. **568**, 052001 (2014).
[11] R. Ishikawa, T. Yamaguchi, Y. Ohtaki, R. Akiyama, and S. Kuroda, J. Cryst. Growth **453**, 124 (2016).
[12] A. A. Taskin, F. Yang, S. Sasaki, K. Segawa, and Y. Ando, Phys. Rev. B **89**, 121302(R) (2014).
[13] B. A. Assaf, F. Katmis, P. Wei, B. Satpati, Z. Zhang, S. P. Bennett, V. G. Harris, J. S. Moodera, and D. Heiman, Appl. Phys. Lett. **105**, 102108 (2014).
[14] K. Zou, S. D. Albright, O. E. Dagdeviren, M. Morales-Acosta, G. H. Simon, C. Zhou, S. Mandal, S. Ismail-Beigi, U. D. Schwarz, E. I. Altman *et al.*, APL Mater. **7**, 051106 (2019).
[15] S. D. Albright, K. Zou, F. J. Walker, and C. H. Ahn, APL Mater. **9**, 111106 (2021).
[16] K. Dybko, G. P. Mazur, W. Wolkanowicz, M. Szot, P. Dziawa, J. Z. Domagala, M. Wiater, T. Wojtowicz, G. Grabecki, and T. Story, arXiv:1812.08711v1.
[17] F. Wei, C.-W. Liu, D. Li, C.-Y. Wang, H.-R. Zhang, J.-R. Sun, X. P. A. Gao, S. Ma, and Z. Zhang, Phys. Rev. B **98**, 161301(R) (2018).
[18] F. Wei, S. Ma, and Z. Zhang, J. Phys. D **52**, 285301 (2019).
[19] J. Liu, W. Duan, and L. Fu, Phys. Rev. B **88**, 241303(R) (2013).
[20] B. A. Assaf, T. Cardinal, P. Wei, F. Katmis, J. S. Moodera, and D. Heiman, Appl. Phys. Lett. **102**, 012102 (2013).
[21] W. A. Beck and J. R. Anderson, J. Appl. Phys. **62**, 541 (1987).
[22] G. Grabecki, A. Dąbrowski, P. Iwanowski, A. Hruban, B. J. Kowalski, N. Olszowska, J. Kołodziej, M. Chojnacki, K. Dybko, A. Łusakowski, T. Wojtowicz, T. Wojciechowski, R. Jakieła, and A. Wiśniewski, Phys. Rev. B **101**, 085113 (2020).
[23] J. Wang, A. Kurzendorfer, L. Chen, Z. Wang, Y. Ando, Y. Xu, I. Miotkowski, Y. P. Chen, and D. Weiss, Appl. Phys. Lett. **118**, 253107 (2021).
[24] A. S. Wadge, G. Grabecki, C. Autieri, B. J. Kowalski, P. Iwanowski, G. Cuono, M. Islam, C. M. Canali, K. Dybko, A. Hruban *et al.*, J. Phys.: Condens. Matter **34**, 125601 (2022).
[25] J. W. McClure, Phys. Rev. **101**, 1642 (1956).
[26] S. Chusnutdinow, S. Schreyeck, S. Kret, A. Kazakov, and G. Karczewski, Appl. Phys. Lett. **117**, 072102 (2020), and references therein.
[27] M. Majewicz, D. Śnieżek, T. Wojciechowski, E. Baran, P. Nowicki, T. Wojtowicz, and J. Wróbel, Acta Phys. Polon. A **126**, 1174 (2014).

[28] S. Hikami, A. I. Larkin, and Y. Nagaoka, Prog. Theor. Phys. **63**, 707 (1980).
[29] M. L. Peres, H. S. Monteiro, V. A. Chitta, S. de Castro, U. A. Mengui, P. H. O. Rappl, N. F. Oliveira, E. Abramof, and D. K. Maude, J. Appl. Phys. **115**, 093704 (2014).
[30] N. Hansen, arXiv:1604.00772 (2016).
[31] M. Nomura, S. Watanabe, Y. Akimoto, Y. Ozaki, and M. Onishi, CoRR arXiv:2012.06932 (2020).
[32] B. L. Altshuler, A. G. Aronov, and D. E. Khmelnitsky, J. Phys. C **15**, 7367 (1982).
[33] H. Fukuyama, Prog. Theor. Phys. Suppl. **69**, 220 (1980).
[34] A. Y. Kuntsevich, N. N. Klimov, S. A. Tarasenko, N. S. Averkiev, V. M. Pudalov, H. Kojima, and M. E. Gershenson, Phys. Rev. B **75**, 195330 (2007).
[35] H.-Z. Lu and S.-Q. Shen, Phys. Rev. B **84**, 125138 (2011).
[36] Y. A. Bychkov and E. I. Rashba, J. Phys. C **17**, 6039 (1984).
[37] I. Garate and L. Glazman, Phys. Rev. B **86**, 035422 (2012).
[38] Y. I. Ravich, B. A. Efimova, and A. Smirnov, *Semiconducting Lead Chalcogenides*, Monographs in Semiconductor Physics (Springer, Boston, 1970).
[39] B. M. Askerov, *Electron Transport Phenomena in Semiconductors* (World Scientific, Singapore, 1994).
[40] Assuming $B \parallel [001]$ and $\mu B \ll 1$, we obtained $\delta^2 = (\gamma^3 - 3\gamma + 2)/[3\gamma(4\gamma^2 + 4\gamma + 1)]$, where $\gamma = m_\parallel/m_\perp$.
[41] J. Antoszewski, D. J. Seymour, L. Faraone, J. R. Meyer, and C. A. Hoffman, J. Electron Mater. **24**, 1255 (1995).
[42] G. Dresselhaus, A. F. Kip, and C. Kittel, Phys. Rev. **98**, 368 (1955).
[43] The motion on a hodograph in momentum space can by converted to an orbit in real space by calculating group velocities $v_x = \partial E(k_x, k_y)/\partial k_x$, $v_y = \partial E(k_x, k_y)/\partial k_y$ and plotting the parametric curve $x(t) = v_x(t)\,t$, $y(t) = v_y(t)\,t$, where t is time.
[44] D. Chrastina, J. P. Hague, and D. R. Leadley, J. Appl. Phys. **94**, 6583 (2003).
[45] P. Virtanen, R. Gommers, T. E. Oliphant, M. Haberland, T. Reddy, D. Cournapeau, E. Burovski, P. Peterson, W. Weckesser, J. Bright *et al.*, Nat. Methods **17**, 261 (2020).
[46] K. S. Stephenson and Y. B. Bazaliy, J. Appl. Phys. **124**, 125103 (2018).
[47] G. Karczewski, M. Szot, S. Kret, L. Kowalczyk, S. Chusnutdinow, T. Wojtowicz, S. Schreyeck, K. Brunner, C. Schumacher, and L. W. Molenkamp, ACS Sym. Ser. **26**, 135601 (2015).
[48] O. A. Aleksandrova, A. T. Akhmedzhanov, R. T. Bondokov, V. A. Moshnikov, I. V. Saunin, Y. M. Tairov, V. I. Shtanov, and L. V. Yashina, Semiconductors **34**, 1365 (2000).
[49] H. Fukuyama, J. Phys. Soc. Jpn. **49**, 644 (1980).
[50] B. L. Altshuler, D. Khmel'nitzkii, A. I. Larkin, and P. A. Lee, Phys. Rev. B **22**, 5142 (1980).
[51] B. L. Altshuler, A. G. Aronov, and P. A. Lee, Phys. Rev. Lett. **44**, 1288 (1980).
[52] S. Datta, *Lessons from Nanoelectronics* (World Scientific, Singapore, 2012).
[53] S. Takaoka, T. Okumura, K. Murase, A. Ishida, and H. Fujiyasu, Solid State Commun. **58**, 637 (1986).
[54] V. Litvinov, Semicond. Sci. Technol. **8**, S364 (1993).
[55] B. Volkov and O. Pankratov, JETP Lett **42**, 178 (1985).
[56] X. Qian, L. Fu, and J. Li, Nano Res. **8**, 967 (2015).
[57] D. M. Mahler, V. L. Müller, C. Thienel, J. Wiedenmann, W. Beugeling, H. Buhmann, and L. W. Molenkamp, Nano Lett. **21**, 9869 (2021).